ADVANCED ENGINEERING MATERIALS
www.aem-journal.com

Synthesis and Characterization of High-Entropy CrMoNbTaVW Thin Films Using High-Throughput Methods

Simon Schweidler, Henrik Schopmans, Patrick Reiser, Evgeniy Boltynjuk, Jhon Jairo Olaya, Surya Abhishek Singaraju, Franz Fischer, Horst Hahn, Pascal Friederich,* and Leonardo Velasco**

High-entropy alloys (HEAs) or complex concentrated alloys (CCAs) offer a huge research area for new material compositions and potential applications. Since the combination of several elements sometimes leads to unexpected and unpredictable material properties. In addition to the element combinations, the optimization of the element proportions in CCAs and HEAs is also a decisive factor in tailoring desired material properties. However, it is almost impossible to achieve the composition and characterization of CCAs and HEAs with a sufficient number of compositions by conventional experiments. Therefore, an optimized high-throughput magnetron sputtering synthesis to fabricate a new HEA gradient layer of six elements is presented. With this approach, the compositional space of the HEA system CrMoNbTaVW can be studied in different subsections to determine the influence of the individual elements and their combinations on the structure, morphology, and physical properties (hardness and resistivity). It is found that the Cr-, Ta-, and W-rich phases, which have a grain size of 10–11 nm, exhibit the hardest mechanical properties, whereas V-, Ta-, and Cr-rich compounds exhibit the highest electrical resistivity. The combination of high-throughput synthesis, automated analysis tools, and automated data interpretation enables rapid and time-efficient characterization of the novel CrMoNbTaVW gradient film.

1. Introduction

Combinatorial materials synthesis, coupled with automated characterization and artificial intelligence techniques, is a promising method for creating materials libraries, i.e., databases that contain relevant information about the chemical composition, crystal structure, microstructure, and properties. However, exploring the infinite possibilities offered by the numerous combinations of elements in the periodic table requires an immense amount of research effort. Promising approaches to explore this infinite combinatorial variety of different material systems can be based on theoretically predicted material combinations, selecting systems based on literature review, or by scientific selections of elements based on experience.

In 1995, Xiang et al. showed the possibilities of creating and screening combinatorial libraries of solid-state compounds using radio frequency sputtering in one of the first papers in the field of combinatorial approach for material discovery.[1] Subsequent pioneering combinatorial

S. Schweidler, P. Reiser, E. Boltynjuk, S. A. Singaraju, F. Fischer, H. Hahn, P. Friederich, L. Velasco
Institute of Nanotechnology
Karlsruhe Institute of Technology
Hermann-von-Helmholtz-Platz 1, 76344 Eggenstein-Leopoldshafen, Germany
E-mail: simon.schweidler@kit.edu; pascal.friederich@kit.edu; lvelascoe@unal.edu.co

The ORCID identification number(s) for the author(s) of this article can be found under https://doi.org/10.1002/adem.202200870.

DOI: 10.1002/adem.202200870

H. Schopmans, P. Friederich
Institute of Theoretical Informatics
Karlsruhe Institute of Technology
Am Fasanengarten 5, 76131 Karlsruhe, Germany

J. J. Olaya
Facultad de Ingeniería
Universidad Nacional de Colombia
Av. Cra. 30 # 45-03, Ed. 407, Ciudad Universitaria, Bogotá D.C. 202017, Colombia

H. Hahn
Joint Research Laboratory Nanomaterials
Technische Universität Darmstadt
Otto-Berndt-Str. 3, 64206 Darmstadt, Germany

L. Velasco
Direccion Academica
Universidad Nacional de Colombia
Sede de La Paz, Km 9 via Valledupar-La Paz, Cesar 202017, Colombia

studies by Ludwig et al. have shown that synthesis techniques such as physical vapor deposition (PVD) can be successfully used to create materials libraries.[2,3] The aforementioned studies were designed to synthesize materials libraries containing no more than five elements, and in the case of PVD, the material libraries were evaluated for three or four elements. In 2004, Ye et al.[4] and Cantor et al.[5] independently published a multicomponent metal alloy containing five different elements in an equiatomic composition and having a single crystal phase. This discovery led to the so-called high-entropy alloys (HEAs). HEAs or high-entropy materials (HEMs) are single-phase multicomponent materials (e.g., metallic or ceramics) with five or more elements in near-equiatomic concentrations. The high configurational entropy (S_{config}) is an important value for judging if the material is a HEM ($S_{\text{config}} > 1.5R$) and it is considered to be the driving force to stabilize a single-phase structure.[6,7] Based on the HEAs, other HEMs have been developed, such as high-entropy oxides, nitrides, carbides, and sulfides, only to name a few.[8–22] In addition, there are many multicomponent systems/materials in the literature that are referred to be high entropic, but not all of them have near equiatomic composition or exhibit significant entropy stabilization. Therefore, other terminologies have been created to include both HEMs (equiatomic and single-phase materials) and non-equiatomic or multiphase systems, such as the so-called complex concentrated alloys (CCAs),[23,24] which are defined as alloys (single or multiphase) containing three or more major elements. In general, the wide area of CCAs and HEMs provides a good starting point for the implementation of materials libraries, since not only the equiatomic composition but also the chemical variations of the constituent elements can lead to sometimes unexpected changes in the material properties. The influence on material properties can mainly be attributed to the so-called cocktail effects, which is one of the four core factors of the high-entropy concept, along with configurational entropy, inertial diffusion, and lattice distortion.[25] As already mentioned, the strongest influence on the material properties results from the elemental composition of the CCAs or HEMs, which specifies the material properties in relation to the elemental interactions. By changing the stoichiometry or the type of incorporated elements, the material can be tailored to desired properties. Of course, the other key factors, such as lattice distortions, also have a significant impact on material properties. For instance, ions of different sizes can cause lattice distortions that can lead to a change in the mechanical and physical properties of a material. The compilation of HEAs and CCAs provided by Gorsse et al. is a guide that can be used to select multicomponent systems of interest.[23] For example, the equiatomic MoNbTaVW system prepared by arc-melting has been shown to be a single-phase and to maintain its chemical homogeneity, even after exposure to high temperatures. It was also found that the high configurational entropy of the MoNbTaVW system could play a crucial role in suppressing the diffusivity of the constituent elements for the accommodation of grain boundary sliding.[26] More recently, the possibility of preparing high-entropy silicides (HES) has been demonstrated for the multicomponent systems $(MoNbTaTiW)Si_2$,[10] $(CrMoNbTaW)Si_2$,[27] and $(CrMoNbTaV)Si_2$[28]; whereas only the latter is a single-phase material with a homogeneous distribution of the constituents. It is important to highlight that in this case [$((CrMoNbTaV)Si_2)$] the CALculation of PHAse Diagrams (CALPHAD) approach was used for prediction.[28] Based on the aforementioned studies on the HEA MoNbTaVW and the HES $(CrMoNbTaV)Si_2$, a multicomponent metallic system based on the metals Cr, Mo, Nb, Ta, V, and W (without silicon) will be synthesized, characterized, and investigated for its properties. The 15 binary phase diagrams of the possible combinations of the six elements (CrMoNbTaVW) show that at least eight binary combinations (Cr–V, Mo–Nb, Mo–Ta, Mo–W, Nb–Ta, Nb–W, Ta–W, and V–W) are solid solutions, three combinations (Cr–Mo, Cr–W, and Mo–V) are solid solutions at temperatures >1000 K, one combination (Nb–V) is a solid solution at temperatures >500 K, and three combinations (Cr–Nb, Cr–Ta, and Ta–V) are expected to form different crystal structures. The new CrMoNbTaVW multicomponent metallic alloy film is synthesized using magnetron sputtering. The experimental setup allows to vary the chemical composition space of the multicomponent system (formation of compositional gradients), to study the crystal structure and morphology, and measure the resistivity and hardness of the none equiatomic compositions, leading to a material library for novel CrMoNbTaVW metal alloys.

2. Results and Discussion

Two CrMoNbTaVW films were prepared, one with a homogeneous equiatomic distribution of elements in a uniformly deposited film and one with a gradient distribution; for simplicity, the equiatomic CrMoNbTaVW multicomponent system and the chemical deviations from the equiatomic system are referred to as CrMoNbTaVW-1 and CrMoNbTaVW-2, respectively, in this manuscript.

Top-view scanning electron microscope (SEM) images at different magnifications, the corresponding chemical composition mapping, and the X-ray diffraction (XRD) patterns in reflection and transmission mode of CrMoNbTaVW-1 are shown in **Figure 1**. The CrMoNbTaVW-1 surface film (Figure 1a,b) exhibits a relatively homogeneous, elongated, pyramidal morphology of crystallites that are free of defects. The XRD patterns acquired in reflection (Figure 1c) and transmission (Figure 1d) show a body-center cubic (BCC) crystal structure (space group *Im*-3*m*). Furthermore, additional peaks from the Si substrate at ≈37° and ≈53° were observed. However, as expected for sputtered BCC films, preferential growth is found in the [110] direction, indicated by the absence of the 200 peaks in the reflection pattern or the weak 200 peaks (≈45°) in the transmission pattern, suggesting that columnar grains are to be expected in the cross-section of the sample. The elemental distribution mapping determined by SEM coupled with energy-dispersive X-ray spectroscopy (EDS) shows a homogeneous distribution within the limits of SEM-EDS characterization (Figure S1, Supporting Information). Taken together, the morphology, crystal structure, and chemical composition of CrMoNbTaVW-1 indicate a solid solution metallic alloy. Although no heat treatments are conducted in this study to fully demonstrate the endothermicity of the sample, it can be assumed that the material belongs to the range of single-phase multicomponent systems.

In the following, the influence of the individual elements on the structural, morphological, and physical properties (hardness

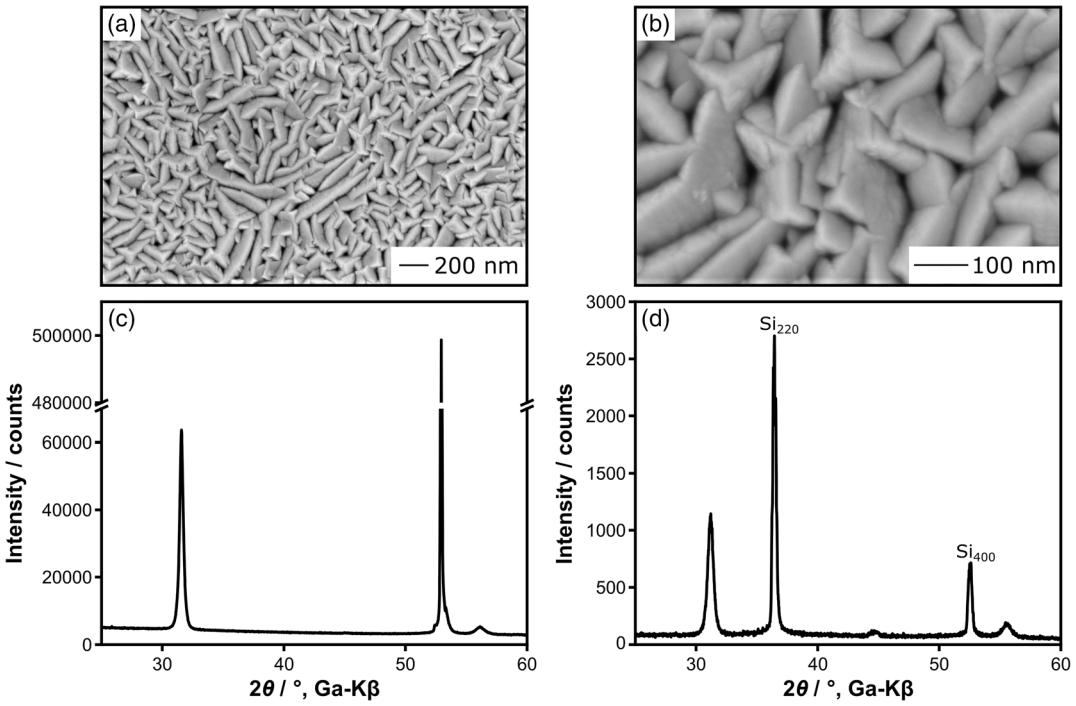

Figure 1. a,b) Top-view scanning electron microscope (SEM) images at different magnifications of CrMoNbTaVW-1. X-ray diffraction (XRD) patterns of CrMoNbTaVW-1 in c) reflection and d) transmission (rotating sample).

and resistivity) will be examined in more detail using the gradient film CrMoNbTaVW-2. **Figure 2** shows the microscopic image of the CrMoNbTaVW-2 (650 images from the 3 inch wafer) together with the arrangement of the sputtering targets, the Si map showing the laser patterning used for SEM-EDS mapping, and the compositional gradient maps of each individual element. To create the material library, the deposition rates of each co-deposited source were adjusted to achieve a near equimolar composition in the center. Chemical compositions were measured using automated high-throughput SEM-EDS on each of the regular $5 \times 5\ mm^2$ measurement grids. Each individual element shows a chemical variation from ≈11 at% (areas of the wafer that are far from the respective sputtered element) to 21 at% (areas of the wafer facing the sputtered element). The color-coded elemental composition maps (Figure 2) show an almost homogeneous distribution of the deposited elements in the center of the wafer. All chemical compositions from different regions (Figure S2, Supporting Information) of CrMoNbTaVW-2 are shown in Table S1, Supporting Information.

For the structural investigation, a total of 157 XRD patterns, one from each of the $5 \times 5\ mm^2$ areas of the wafer, were acquired using an automated XRD device (**Figure 3**, all XRD patterns are

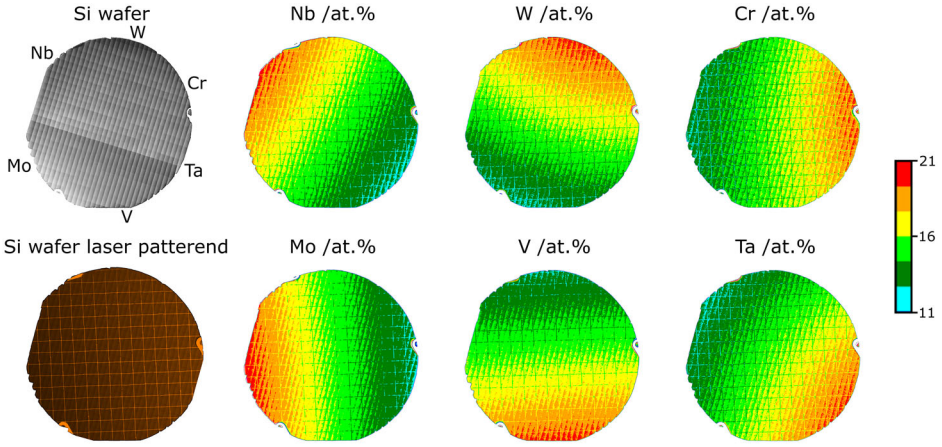

Figure 2. Reconstruction of a 3 inch silicon wafer from 650 microscopic images together with the laser patterned Si wafer and the chemical composition maps for sample CrMoNbTaVW-2. The chemical composition for each of the elements varies from 11–21 at%.

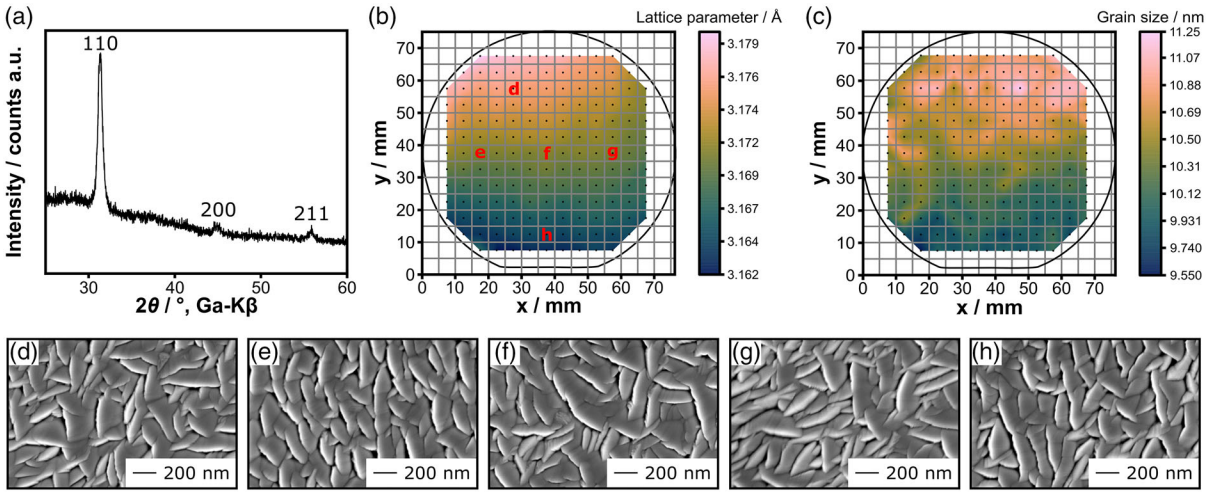

Figure 3. a) Example XRD diagram of the nearly equimolar CrMoNbTaVW-2 combination from the center of the wafer and contour plots of the: b) lattice parameters, c) the grain sizes of all CrMoNbTaVW-2 gradients, and d–h) top-view SEM images of the regions highlighted in b).

displayed in the Supporting Information Library and the raw data can be found in Supporting Information Data). The orientation of the wafer in Figure 3b,c is similar to that in Figure 2. The XRD pattern from the center of the wafer (elements in near equiatomic amounts) shows that this region appears to be a single-phase (Figure 3a). Three peaks (strong 110, weak 200, and 211 peaks) belonging to the BCC structure (space group *Im*-3*m*) are observed, clearly showing preferential growth in the [110] direction; the same applies to all the other 156 regions (see Supporting Information Library and Supporting Information Data). Figure 3b,c show the contour plots of the lattice parameters (LP) and the grain size (GS) distribution for the different compositions of the CrMoNbTaVW-2 sample, respectively. Although the range of LP change is very small, on the order of ≈0.2 Å, it is noticeable that the material regions with higher Nb and/or W content have larger LP, whereas Mo- and V-rich regions have the smallest LP. However, a more significant difference was observed for the GSs. The Nb- and W-rich regions have the largest GS, whereas the V-rich compositions have the smallest GS. As each area appears to form a solid solution, it can be assumed that the LP follows Vegard's law. For this purpose, the average LP based on the chemical composition determined at seven different locations on the wafer was calculated (Table S2, Supporting Information). The calculated LP varies between ≈3.14 and 3.15, which is relatively close to the experimental results (Figure 3b).

To investigate the possible influence of small, medium, and large LP and GS on the morphology, the surface structure at the respective locations was examined in more detail using SEM (Figure 3d–h). All regions show an elongated pyramidal morphology of crystallites and are free of defects and pores, as already observed for CrMoNbTaVW-1. Furthermore, there are no significant differences in morphology between the investigated areas.

In the next step, automated hardness and resistivity measurements were performed to determine the properties of the novel CrMoNbTaVW thin film gradients to provide indications of potential application areas. The hardness and resistivity measurement results from the CrMoNbTaVW-2 sample are shown in **Figure 4**a,b, respectively. Figure 4c,d, shows a top-view SEM image of the nanoindentation of the hardest sample region and the corresponding indentation curve, respectively. The hardness contour plot shows that the equimolar composition region (center of the wafer) and the regions rich in W, Cr, and Ta have the highest mechanical hardness, whereby the Cr- and Ta-rich areas exhibit a slightly higher hardness than the W-rich compositions. Upon closer examination, it is noticeable that the material compositions with a high Cr, Ta, and W content and an average GS between 10 and 11 nm exhibit the highest hardness. In contrast, the V-rich material composition region shows the lowest hardness. As the XRD results of all investigated areas did not show any secondary phases (Supporting Information Library), it can be assumed that a solid solution has formed in the gradients of the CrMoNbTaVW-2 thin film. Therefore, the changes in hardness are probably due to the solidification of the solid solution. The theory on strengthening in solid solutions, already described by Fleischer[29] in 1963 and further developed by Labusch,[30] correlates the concentration of a solute to the resulting increase in strength by a solid solution hardness coefficient. In general, the increase in strength in solid solution is due to the interaction of lattice dislocations with solutes. Substitutional solutes can thus cause a geometric (due to size differences) as well as chemical (different binding energies) distortion in the lattice. The movement of a dislocation is hindered by these lattice distortions so that an additional resolved shear stress is required for further plastic deformation. Therefore, it is generally valid that the hardness of a material increases with decreasing GS (see Hall–Petch effect).[31–33] The CrMoNbTaVW material compositions with the smallest GS were supposed to have the highest hardness, but this is not the case. However, our results are consistent with the study of Fen et al. on the size effect on the mechanical properties of nanocrystalline NbMoTaW thin films.[34] The high-entropy BCC–NbMoTaW alloy films exhibited the highest hardness (≈16.0 GPa) at a GS of ≈10 nm. With increasing GS or film thickness, the hardness decreased and below the critical GS (<10 nm) the material became progressively softer.[34] Furthermore, the theoretical

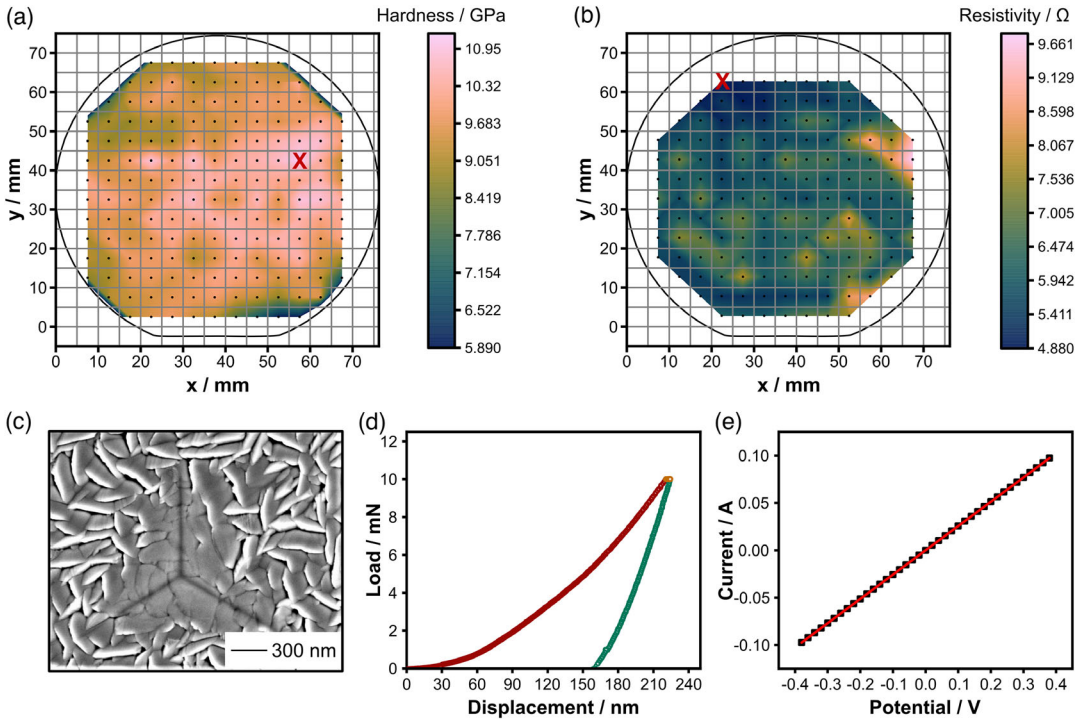

Figure 4. Contour plots of the: a) hardness and b) resistivity of the CrMoNbTaVW-2 sample. c) Example of a top-view SEM image of a hardness indentation with the d) corresponding nanoindentation force curve of the hardest region highlighted by red X in a). e) Example of a resistivity measurement on the sample with the lowest resistance (marked by a red X in b).

and practical work of Wu et al. on Cr_xFeNiCu metal alloys shows that, the proportion of the BCC phase increases with increasing Cr content and that an increase in Cr content can lead to a reduction in GS and thus to an increase in hardness.[35] A similar behavior was also observed by Geanta et al. for AlCrFeCoNi high-entropy metal alloys with varying Cr content.[36] Furthermore, it was shown that incorporation and increasing of the W or Ta content in multicomponent metals (e.g., W_xTaTiVCr or $(Cr_{0.33}Fe_{0.33}V_{0.33})_x(Ta_{0.5}W_{0.5})_{100-x}$), results in an increase in hardness properties.[37–41] Surprisingly, it might be expected that a higher Mo content would also lead to an increase in the hardness of the multicomponent materials, since pure molybdenum has a hardness of ≈12 GPa, which is in the same range as Ta (12 GPa) and W (14 GPa).[42] However, as mentioned earlier, the GS of the Mo-rich materials is <10 nm, likely below a critical size for the inverse Hall–Petch effect,[43] so the hardness is lower than the Cr-, Ta-, or W-rich compositions. The assumption that crystallite size has a significant influence on hardness properties is confirmed when considering areas with increased V (GS < 10 nm) and Nb (GS > 10 nm) content. Although pure vanadium is about two times harder[44] than pure Nb (3 GPa),[34] areas with increased V content exhibit lower hardness compared to areas with increased Nb content. Accordingly, the combination of low hardness (compared to Mo, Ta, Cr, and W) and GS < 10 nm leads to the lowest hardness of the entire wafer for V-rich areas. It can therefore be assumed that, in addition to the selection of the incorporated materials that can influence the GS, the GS itself has a much greater influence on the hardness properties of the multicomponent materials.[34]

Figure 4b shows the contour plot of the resistivity measurements for the CrMoNbTaVW-2 high-entropy thin film sample. Figure 4e depicts, exemplary, the vertical and horizontal 4-point resistance of one of the $5 \times 5\,mm^2$ sheets. Equation (2) (see Experimental Section) was used to calculate the sheet resistance, which was 4.9 Ω. Similarly, the resistances were determined for all other material compositions in the respective squares. The resistivities varied only slightly between 4.9 and 9.4 Ω across the high-entropy gradient thin film (Figure 4b). The slight change is probably due to the leakage current associated with small variations in the positioning of the measurement tips on the sample. However, the resistivity measurements confirm that low resistance is present, confirming the metallic nature of the HEA film. In addition, the data show that the materials with a high V, Ta, and Cr content have the highest resistivity, which in turn is relatively close to the resistivities of the pure metals. As V, Ta, and Cr generally have higher resistivities in contrast to Mo or V. However, it should be taken into account that due to the mixtures possible modifications of the electrical resistance can arise, which are not foreseeable. An assessment of the influence of the various elements in the material compositions on the electrical resistivity would be possible with simulation studies, but this is outside the scope of this work. In addition, we would like to point out to the reader that the HEA used in the present study was selected based on literature review and experience. However, it is of utmost importance to introduce methodologies that are based on computational design (e.g., CALPHAD).[45] Nevertheless, careful attention should be paid to the difference that exists between film and bulk materials.

For instance, in terms of the microstructure, the crystallographic orientation in thin films (e.g., the preferred orientation or GS as shown here) may differ from that of the one in the same bulk material, as has been observed for example in magnesium alloys.[46] The associated crystallographic changes (e.g., GS) can then have either a positive or a negative effect on the properties and potential applications. A next step to extend the material library for the CrMoNbTaVW composition could be to increase the total number of additional gradient compositions by varying the target positions. This could be beneficial, as different mixing ratios (cocktail effects) could lead to additional unexpected material properties and thus application areas that are not predictable.

3. Conclusion

In this study, a material library of single-phase high-entropy metals with spread composition was created by combinatorial synthesis using six metals Cr, Mo, Nb, Ta, V, and W. The composition gradients of the CrMoNbTaVW thin film were investigated using high-throughput SEM/EDS. The microstructure examination showed a homogeneous distribution of the elements without any element segregation for both samples CrMoNbTaVW-1 and CrMoNbTaVW-2. In the gradient film of CrMoNbTaVW-2, an equimolar composition of the different elements was observed in the center of the wafer. In the other parts of the gradient film, the composition in each of the studied areas ($5 \times 5\ mm^2$) was within a range of variation of 11–21 at% of the individual elements. The change in the LP seems to follow Vegard's law. The CrMoNbTaVW-2 compositions with high Cr, W, and Ta content showed the highest hardness, whereas with higher Mo, Nb, and V content the hardness property decreased. The different degrees of hardness can be correlated with the GS. It seems that the materials with a GS of 10–11 nm have a harder mechanical property. In addition, a higher proportion of Cr, W, and Ta also leads to an increase in mechanical hardness. The resistance measurements show a narrow resistance window for the different gradients of 4.9–9.4 Ω, confirming the metallic character of the CrMoNbTaVW HEA.

4. Experimental Section

Combinatorial Synthesis: Single-sided polished silicon <100> wafers (385 µm thickness, Microchemicals GmbH) were used for the deposition of CrMoNbTaVW-1 ($20 \times 20\ mm^2$) and CrMoNbTaVW-2 (3 inch diameter) films. The simultaneous sputtering deposition was performed in a large distance magnetron sputtering system with an octagonal geometry (CreaTec Fischer & Co. GmbH) that could contain up to eight 3 inch targets. The sputtering chamber was optimized for co-sputter deposition with a target-to-substrate distance of 285 mm. The magnetrons were tilted at an angle of 37.5° relative to the *Z* axis. The silicon substrates were positioned in the center of the XY axis of the chamber and −4 cm off-axis in the *Z* direction to enhance gradient deposition specifically for the CrMoNbTaVW-2 sample. The Cr, Mo, V, and W targets (purities 99.99%) were connected to direct current power supplies at powers of 69, 87, 143, and 77 W, respectively, and the Nb and Ta targets (purities 99.99%) were connected to radiofrequency power supplies at powers of 225 and 157 W, respectively. Prior to deposition, the chamber was first evacuated to 4×10^{-10} mbar. The deposition was performed at a constant argon flow of 40 sccm and a working pressure of 3×10^{-3} mbar. The deposition time was 120 min. For CrMoNbTaVW-1, the substrate was rotated at 20 rpm to obtain a homogeneous, uniform film, while for CrMoNbTaVW-2, the substrate was not rotated (gradient formation); the average thickness of each film was ≈1.5 µm.

Laser Patterning: Squares of $5 \times 5\ mm^2$ and a depth of ≈10 µm were laser patterned on CrMoNbTaVW-2 after deposition using a TruMicro 5000 laser ablation system (TRUMPF SE + Co. KG). The picosecond laser beam had a diameter of 20 µm and a laser frequency of 800 kHz. For optimal patterning, the laser power was set to 2.5 W. A vacuum pump was used to prevent nanoparticles from being deposited on the substrate during patterning.

Chemical Composition: An SEM (LEO 1530, Carl Zeiss AG) equipped with an EDS detector (Oxford Instruments) was used to examine the morphology and determine the chemical composition of the samples (using AZTEC software, Oxford, Instruments). The acceleration voltage and the working distance were 20 kV and 8.5 mm, respectively. The mapped area of the CrMoNbTaVW-2 sample consists of the reconstruction of 650 individual scans, each scan covers an area of $3.27 \times 2.45\ mm^2$ and the resolution for data acquisition was 256×192 pixels (each pixel size ≈12.7 µm).

X-ray Diffraction: Automated XRD experiments for the CrMoNbTaVW-2 sample were performed in an STOE Stadi P diffractometer equipped with a Ga-jet X-ray source (Ga-Kβ radiation, 1.207930 Å), with a spot size of ≈200 µm, and an in-house modified XY stage for automated sample measurements. A total of 169 X-ray diffractograms (XRDs) were acquired for CrMoNbTaVW-2, each at the center of the $5 \times 5\ mm^2$ laser patterned areas. All X-ray diffractograms were taken in transmission mode. For comparison, the CrMoNbTaVW-1 sample was also investigated using the STOE Stadi P diffractometer (Ga-jet X-ray source), and the XRD data were recorded in transmission and reflection mode (the sample was kept rotating during measurements).

Automated XRD Analysis: The baseline of the diffractograms was subtracted using asymmetrically reweighted penalized least squares smoothing (arPLS)[46] with parameters ratio = 0.1 and $\lambda = 10^{-7}$. The positions of the peaks of interest were obtained after subsequent smoothing using a moving average with a window width of 1.5°. Gaussian profiles were fitted to the peaks of the baseline-corrected diffractogram to extract the relevant parameters. All results of this automatic adjustment process could be found in the Supporting Information Library and in the Supporting Information Data.

Resistivity Measurements: Four-point sheet resistance measurements were made using the van der Pauw method with an Agilent 4156C parameter analyzer (Agilent Technologies GmbH). The resistivity for each sample was determined from the $5 \times 5\ mm^2$ areas patterned on the CrMoNbTaVW-2 sample. For comparison, the resistance of the sample CrMoNbTaVW-1 was also measured. The sheet resistance, R_s is calculated after measuring the vertical (R_V) and horizontal (R_H) resistances of each square, and the relation was given by the van der Pauw equation[47]

$$e^{\frac{-\pi R_V}{R_S}} + e^{\frac{-\pi R_H}{R_S}} = 1 \tag{1}$$

When $R_H = R = R_V$, the sheet resistance is given by

$$R_S = \frac{\pi R}{\ln 2} \tag{2}$$

Hardness Measurements: The hardness was determined using a Nano Indenter G200 XP (Agilent Technologies GmbH) equipped with a diamond Berkovich tip. Prior to measurements, the instrument was calibrated using a standard fused silica reference sample. Measurements were performed at room temperature in load control mode with a peak load of 10 mN at a strain rate of 0.05 s^{-1} and a dwell time of 10 s at maximum load. For each of the $5 \times 5\ mm^2$ areas, 10 indentations were conducted, giving a total of 1640 indentations. The nanoindenter tip was recalibrated every 500 measurements to guarantee the sharpness of the tip and the validity of the data obtained. Values of hardness were calculated using the Oliver–Pharr method.[48]

Supporting Information

Supporting Information is available from the Wiley Online Library or from the author.

Acknowledgements

S.S. acknowledges the support from EPISTORE project funded by the European Union's Horizon 2020 research and innovation program under grant agreement no. 101017709.

Correction added on 11 October 2022, after first online publication: Projekt Deal funding statement has been added.

Open access funding enabled and organized by Projekt DEAL.

Conflict of Interest

The authors declare no conflict of interest.

Data Availability Statement

The data that support the findings of this study are available in the supplementary material of this article.

Keywords

DC sputtering, hardness, high-entropy materials, high-throughput, materials libraries, phase diagram, resistivity

Received: June 16, 2022
Revised: August 26, 2022
Published online:

[1] X. D. Xiang, X. Sun, G. Briceño, Y. Lou, K. A. Wang, H. Chang, W. G. Wallace-Freedman, S. W. Chen, P. G. Schultz, *Science* **1995**, *268*, 1738.
[2] A. Ludwig, *npj Comput. Mater.* **2019**, *5*, 70.
[3] A. Ludwig, R. Zarnetta, S. Hamann, A. Savan, S. Thienhaus, *Z. Met. Res. Adv. Technol.* **2008**, *99*, 1144.
[4] J. W. Yeh, S. K. Chen, S. J. Lin, J. Y. Gan, T. S. Chin, T. T. Shun, C. H. Tsau, S. Y. Chang, *Adv. Eng. Mater.* **2004**, *6*, 299.
[5] B. Cantor, I. T. H. Chang, P. Knight, A. J. B. Vincent, *Mater. Sci. Eng. A* **2004**, *375–377*, 213.
[6] C. M. Rost, E. Sachet, T. Borman, A. Moballegh, E. C. Dickey, D. Hou, J. L. Jones, S. Curtarolo, J. P. Maria, *Nat. Commun.* **2015**, *6*, 8485.
[7] B. S. Murty, J. W. Yeh, S. Ranganathan, P. P. Bhattacharjee, *High-Entropy Alloys*, Elsevier Science, Netherlands **2019**.
[8] J. Wang, Y. Cui, Q. Wang, K. Wang, X. Huang, D. Stenzel, A. Sarkar, R. Azmi, T. Bergfeldt, S. S. Bhattacharya, R. Kruk, H. Hahn, S. Schweidler, T. Brezesinski, B. Breitung, *Sci. Rep.* **2020**, *10*, 18430.
[9] D. Bérardan, S. Franger, D. Dragoe, A. K. Meena, N. Dragoe, *Phys. Status Solidi - Rapid Res. Lett.* **2016**, *10*, 328.
[10] L. Lin, K. Wang, R. Azmi, J. Wang, A. Sarkar, M. Botros, S. Najib, Y. Cui, D. Stenzel, P. A. Sukkurji, Q. Wang, H. Hahn, S. Schweidler, B. Breitung, *J. Mater. Sci.* **2020**, *55*, 16879.
[11] Q. Wang, A. Sarkar, D. Wang, L. Velasco, R. Azmi, S. S. Bhattacharya, T. Bergfeldt, A. Düvel, P. Heitjans, T. Brezesinski, H. Hahn, B. Breitung, *Energy Environ. Sci.* **2019**, *12*, 2433.
[12] C. Duan, X. Li, D. Wang, Z. Wang, H. Sun, R. Zheng, Y. Liu, *Sustainable Energy Fuels* **2022**, *6*, 1479.
[13] S. Jiang, T. Hu, J. Gild, N. Zhou, J. Nie, M. Qin, T. Harrington, K. Vecchio, J. Luo, *Scr. Mater.* **2018**, *142*, 116.
[14] A. Sarkar, B. Eggert, L. Velasco, X. Mu, J. Lill, K. Ollefs, S. S. Bhattacharya, H. Wende, R. Kruk, R. A. Brand, H. Hahn, *APL Mater.* **2020**, *8*, 051111.
[15] R. Djenadic, A. Sarkar, O. Clemens, C. Loho, M. Botros, V. S. K. Chakravadhanula, C. Kübel, S. S. Bhattacharya, A. S. Gandhi, H. Hahn, *Mater. Res. Lett.* **2017**, *5*, 102.
[16] A. Sarkar, R. Djenadic, D. Wang, C. Hein, R. Kautenburger, O. Clemens, H. Hahn, *J. Eur. Ceram. Soc.* **2018**, *38*, 2318.
[17] Y. Ma, Y. Ma, S. L. Dreyer, Q. Wang, K. Wang, D. Goonetilleke, A. Omar, D. Mikhailova, H. Hahn, B. Breitung, T. Brezesinski, *Adv. Mater.* **2021**, *33*, 2101342.
[18] J. Gild, J. Braun, K. Kaufmann, E. Marin, T. Harrington, P. Hopkins, K. Vecchio, J. Luo, *J. Mater.* **2019**, *5*, 337.
[19] D. Stenzel, I. Issac, K. Wang, R. Azmi, R. Singh, J. Jeong, S. Najib, S. S. Bhattacharya, H. Hahn, T. Brezesinski, S. Schweidler, B. Breitung, *Inorg. Chem.* **2021**, *60*, 115.
[20] C. Oses, C. Toher, S. Curtarolo, *Nat. Rev. Mater.* **2020**, *5*, 295.
[21] L. Lin, K. Wang, A. Sarkar, C. Njel, G. Karkera, Q. Wang, R. Azmi, M. Fichtner, H. Hahn, S. Schweidler, B. Breitung, *Adv. Energy Mater.* **2022**, *2103090*, 2103090.
[22] R. Z. Zhang, F. Gucci, H. Zhu, K. Chen, M. J. Reece, *Inorg. Chem.* **2018**, *57*, 13027.
[23] S. Gorsse, J. P. Couzinié, D. B. Miracle, *C. R. Phys.* **2018**, *19*, 721.
[24] K. Chen, X. Pei, L. Tang, H. Cheng, Z. Li, C. Li, X. Zhang, L. An, *J. Eur. Ceram. Soc.* **2018**, *38*, 4161.
[25] J. W. Yeh, *JOM* **2013**, *65*, 1759.
[26] A. Xia, R. Franz, *Coatings* **2020**, *10*, 941.
[27] D. Liu, Y. Huang, L. Liu, L. Zhang, *Mater. Lett.* **2020**, *268*, 127629.
[28] A. L. Vyatskikh, B. E. MacDonald, A. D. Dupuy, E. J. Lavernia, J. M. Schoenung, H. Hahn, *Scr. Mater.* **2021**, *201*, 113914.
[29] R. L. Fleischer, *Acta Metall.* **1963**, *11*, 23.
[30] R. Labusch, *Phys. Status Solidi* **1970**, *41*, 659.
[31] E. O. Hall, *Proc. Phys. Soc. Sect. B* **1951**, *64*, 747.
[32] N. J. Petch, *J. Iron Steel Inst.* **1953**, *174*, 25.
[33] J. D. Eshelby, F. C. Frank, F. R. N. Nabarro, *London, Edinburgh, Dublin Philos. Mag. J. Sci.* **1951**, *42*, 351.
[34] X. B. Feng, J. Y. Zhang, Y. Q. Wang, Z. Q. Hou, K. Wu, G. Liu, J. Sun, *Int. J. Plast.* **2017**, *95*, 264.
[35] H. Wu, S. Huang, C. Zhu, H. Zhu, Z. Xie, *Prog. Nat. Sci.: Mater. Int.* **2020**, *30*, 239.
[36] V. Geantă, I. Voiculescu, B. Istrate, D. M. Vrânceanu, R. Ciocoiu, C. M. Cotruț, *Int. J. Eng. Res. Afr.* **2018**, *37*, 23.
[37] Z. Wu, W. Guo, K. Jin, J. D. Poplawsky, Y. Gao, H. Bei, *J. Mater. Res.* **2018**, *33*, 3301.
[38] Y. Chen, Y. Fang, X. Fu, Y. Lu, S. Chen, H. Bei, Q. Yu, *J. Mater. Sci. Technol.* **2021**, *73*, 101.
[39] O. A. Waseem, H. J. Ryu, *Sci. Rep.* **2017**, *7*, 1926.
[40] M. Zhang, B. Yang, J. Chu, T. G. Nieh, *Scr. Mater.* **2006**, *54*, 1227.
[41] Q. Xing, J. Ma, Y. Zhang, *Int. J. Miner., Metall. Mater.* **2020**, *27*, 1379.
[42] H. Kim, S. Nam, A. Roh, M. Son, M. H. Ham, J. H. Kim, H. Choi, *Int. J. Refract. Met. Hard Mater.* **2019**, *80*, 286.
[43] C. E. Carlton, P. J. Ferreira, *Acta Mater.* **2007**, *55*, 3749.
[44] M. A. Mamun, K. Zhang, H. Baumgart, A. A. Elmustafa, *Appl. Surf. Sci.* **2015**, *359*, 30.
[45] Q. Wang, L. Velasco, B. Breitung, V. Presser, *Adv. Energy Mater.* **2021**, *11*, 2102355.
[46] K. Schlüter, C. Zamponi, A. Piorra, E. Quandt, *Corros. Sci.* **2010**, *52*, 3973.
[47] L. J. van der Pauw, *Philip Res. Repts* **1958**, *13*, 1.
[48] W. C. Oliver, G. M. Pharr, *J. Mater. Res.* **1992**, *7*, 1564.